

# Microscale Correlations Adoption in Solid Oxide Fuel Cell

C. Wang<sup>1</sup>

Mechanical and Materials  
Engineering Department,  
Wright State University,  
3640 Colonel Glenn Highway,  
Dayton, OH 45435  
e-mail: chao.wang@wright.edu

*In order to develop a predictive model of real cell performance, firm relationships and assumptions need to be established for the definition of the physical and microstructure parameters for solid oxide fuel cells (SOFCs). This study explores the correlations of microstructure parameters from a microscale level, together with mass transfer and electrochemical reactions inside the electrodes, providing a novel approach to predict SOFC performance numerically. Based on the physical connections and interactions of microstructure parameters, two submodel correlations (i.e., porosity–tortuosity and porosity–particle size ratio) are proposed. Three experiments from literature are selected to facilitate the validation of the numerical results with experimental data. In addition, a sensitivity analysis is performed to investigate the impact of the adopted submodel correlations to the SOFC performance predictions. Normally, the microstructural inputs in the numerical model need to be measured by experiments in order to test the real cell performance. By adopting the two submodel correlations, the simulation can be performed without obtaining relatively hard-to-measure microstructural parameters such as tortuosity and particle size, yet still accurately mimicking a real-world well-structured SOFC operation. By accurately and rationally predicting the microstructural parameters, this study can eventually help to aid the experimental and optimization study of SOFC. [DOI: 10.1115/1.4031153]*

**Keywords:** solid oxide fuel cell, numerical performance predictions, microstructure parameter correlations, sensitivity analysis

## 1 Introduction

In order to investigate SOFCs mathematically, a significant amount of effort [1–7] has been placed toward development of models including mass transportation and electrochemical reactions. Zhu et al. [1] presents a new computational modeling framework for SOFC simulation that takes the whole system including flow channels and planar membrane-electrode assemblies into consideration. His work employed multistep reaction mechanisms in terms of detailed elementary heterogeneous chemical kinetics. Detailed charge transfer reactions are analyzed by separating the mechanism into several elementary steps. Greene et al. [2] focuses on minimizing the concentration overpotential by applying functionally graded electrodes (FGEs) and observes the physical phenomenon of mass transfer throughout the electrodes for multigas inputs. However, the activation overpotential in both of their models is directly calculated by the Butler–Volmer equation and does not take the microstructural characteristics into consideration. Theoretically, these microstructural factors are critical to the size of active reaction surface sites and hence affect the rate of electrochemical reaction. Ni et al. [3] developed the model from a microscale level, and the model was able to capture the coupled electrochemical reactions and mass transfer involved in SOFC operation. However, the microstructural parameters are treated separately despite the fact these parameters are observed to physically correlate with each other. For instance, when one parameter changes the rest of the parameters should alter correspondingly.

The primary focus of our work is to investigate how the microstructural parameters are related to each other and how they affect cell performance. Several studies associated with tortuosity and porosity relations were developed and organized by Matyka et al. [8]. For a spherical particle mixture, Currie [9] proposed that

porosity is inversely proportional to tortuosity. This assumption was confirmed by experimental data. Dias et al. [10] extended this study and investigated the adjustable parameter,  $n$ , which is crucial to determining the porosity–tortuosity correlation (see Eq. (31)). German [11] summarized that porosity, relative composition of two species, and the particle size ratio in a binary mixture of spherical particles are dependent on each other. The larger the particle size ratio is (i.e., the larger the difference between the sizes of the two particles), the higher the packing density at all compositions will be. Dias et al. [12] explored the dependence of packing porosity on particle size ratio, focusing on exploring the significance of particle size ratio. These complex interrelating factors can be important in the accuracy of a predictive SOFC model. It should be noted that SOFC fabrication technology including tape casting, screen printing, spray deposition, etc., has been very well developed in recent years. It is applicable and realistic for the experimentalists to alter the size of the particles, composition of ionic and electronic conductors, or porosity during the fabrication process. To take advantage of that, FGEs have been applied to SOFCs aiming to improve the cell performance by using graded porosity, particle size, or composition of electronic and ionic conductors throughout the electrodes. The advantages of FGEs include expanding the electrochemical reaction area, optimizing the electrical/ionic conductivity, improving the gas transport, and reducing operating temperatures. It can be seen that the microstructure parameters we will try to vary in numerical study can also be adjusted in real experimentations. This also proves that this numerical study has practical significance.

The aim of this paper is to expand upon previously developed theories and models [4,5] and develop a new method that takes into account electronic, ionic, and gas transport together with electrochemical reaction effects. It can predict the distribution of overpotentials, current densities, and gas concentrations along the electrode. Also, the model takes into account all the microstructural factors that are critical to cell performance. In addition, the model applies the binary random packed sphere model to mimic the microstructural make-up in the electrodes [6,7]. Most importantly, this study aims to explore

<sup>1</sup>Corresponding author.

Contributed by the Advanced Energy Systems Division of ASME for publication in the JOURNAL OF FUEL CELL SCIENCE AND TECHNOLOGY. Manuscript received December 16, 2014; final manuscript received July 21, 2015; published online August 18, 2015. Assoc. Editor: Dr Masashi Mori.

the correlations of the key microstructural parameters of SOFC, such as porosity, tortuosity, and particle size by utilizing an existing numerical model as a media. To the best of the author's knowledge, an exploration on the correlation of microstructural parameters is absent in the literature, which is crucial to resemble a real-world cell performance. By studying the feasibility of involving the microstructure parameters correlations, together with model validation and sensitivity analysis, we aim to exhibit a new perspective for numerical simulation of SOFC.

## 2 Numerical Model

### 2.1 Anode

**2.1.1 Overpotential Due to Electrochemical Reactions and Ohmic Resistance.** The overall charge balance relationship can be written as

$$\frac{dJ_{e,a}}{dx} = -\frac{dJ_{i,a}}{dx} = -S_v J_{n,a} \quad (1)$$

where  $J_{e,a}$  and  $J_{i,a}$  are the current density (A/m<sup>2</sup>) due to transport of electronic and ionic conductors in the anode,  $S_v$  is active surface area per unit volume (m<sup>2</sup>/m<sup>3</sup>) of the porous electrode, and  $J_{n,a}$  is the transfer current density per unit area of reaction surface (A/m<sup>2</sup>). This equation accounts for the electrochemical reaction rate for the fuel cell along the anode.

The active surface area per unit volume indicates the available reaction sites that can be used for electrochemical reactions and was developed by Costamagna et al. [7] from binary random packing and percolation theories. It is represented by

$$S_v = \pi \sin^2 \theta r_e^2 n_t n_i n_e \frac{Z_e Z_i}{6} P_i P_e \quad (2)$$

where  $\theta$  is the contact angle between electronic and ionic conducting particles,  $r_e$  is the radius of electronic conducting particles,  $n_t$  is the total number of particles per unit volume,  $n_i$  and  $n_e$  are the number fraction of ionic and electronic conducting particles, respectively,  $Z_i$  and  $Z_e$  are the coordination number of ionic and electronic conducting particles, respectively, and  $P_i$  and  $P_e$  are the probability that a given ionic or electronic conducting particle, respectively, belongs to a percolation cluster. Essentially,  $S_v$  can be expressed as a function of porosity, electronic particle size, number fraction, and particle size ratio [7]. This model shows good agreement with literature experimental data by assuming electrode formed by a mixture of electronic and ionic conductors with spherical particle shape to approximate the real cell structure. It can be seen from Fig. 1 that percolating (or A-) cluster is a cluster of particles of the same type that extends through the entire thickness of the electrode. On the other hand, B- and C-clusters are not entirely connected because B-clusters are short networks connected only to the respective collector while C-clusters are completely isolated. The probability of connection P, i.e., the probability that a generic electronic (or ionic) particle belongs to a percolating cluster of the same kind of particles, essentially depends on the volume fraction (or number fraction) and particle size ratio [7].

The transfer current density is normally described by the general form of the Butler–Volmer (B–V) equation given by

$$J_{n,a} = J_{0,a} \left\{ \frac{y_{H_2}}{y_{H_2}'} \exp\left(\frac{\beta z F \eta_a}{RT}\right) - \frac{1 - y_{H_2}}{1 - y_{H_2}'} \exp\left(-\frac{(1 - \beta) z F \eta_a}{RT}\right) \right\} \quad (3)$$

where  $J_{0,a}$  is the exchange current density of the anode (A/m<sup>2</sup>),  $y_{H_2}$  is the molar fraction of H<sub>2</sub>,  $y_{H_2}'$  is the molar fraction of H<sub>2</sub> at the fuel channel,  $R$  is the ideal gas constant (8.314 J/mol K),  $T$  is

the operating temperature (K), and  $\beta$  is the charge transfer coefficient and is normally chosen to be 0.5 for symmetry [13].

Applying Ohm's law for the electronic and ionic conductors, we get

$$\frac{dV_e}{dx} = \rho_{e,a}^{\text{eff}} J_{e,a}; \quad \frac{dV_i}{dx} = \rho_{i,a}^{\text{eff}} J_{i,a} \quad (4)$$

$\rho_{e,a}^{\text{eff}}$  is the effective resistivity ( $\Omega$  m) of the anode electronic conductors;  $\rho_{i,a}^{\text{eff}}$  is the effective resistivity of anode ionic conductors; and  $V_e$  and  $V_i$  are the electronic and ionic potential (V), respectively. The effective resistivity can be determined as

$$\rho_{e,a}^{\text{eff}} = \frac{\tau}{\phi_e (1 - \varepsilon) \sigma_{e,a}} \quad (5a)$$

$$\rho_{i,a}^{\text{eff}} = \frac{\tau}{(1 - \phi_e)(1 - \varepsilon) \sigma_{i,a}} \quad (5b)$$

where  $\phi_e$  is the volume fraction of electronic conductors,  $\tau$  is tortuosity of the anode,  $\varepsilon$  is porosity of the anode,  $\sigma_{e,a}$  is the electronic conductivity (S/m) of the anode electronic conductors, and  $\sigma_{i,a}$  is ionic conductivity (S/m) of the anode ionic conductors.

The anode overpotential  $\eta_a$  can be determined by the difference of equilibrium potential and practical potential is given as

$$\eta_a = (V_e^{\text{eq}} - V_i^{\text{eq}}) - (V_e - V_i) \quad (6)$$

where  $V_e^{\text{eq}}$  and  $V_i^{\text{eq}}$  are the equilibrium electronic and ionic potential (V), respectively, and are constant throughout the cell.

The first derivative of  $\eta_a$  can be written as

$$\frac{d\eta_a}{dx} = -\left(\frac{dV_e}{dx} - \frac{dV_i}{dx}\right) = \rho_{i,a}^{\text{eff}} J_{i,a} - \rho_{e,a}^{\text{eff}} J_{e,a} \quad (7)$$

Combining the charge balance and B–V equation, the second derivative of  $\eta_a$  is equal to

$$\begin{aligned} \frac{d^2 \eta_a}{dx^2} &= \rho_{i,a}^{\text{eff}} \frac{dJ_{i,a}}{dx} - \rho_{e,a}^{\text{eff}} \frac{dJ_{e,a}}{dx} = S_v J_{n,a} (\rho_{i,a}^{\text{eff}} + \rho_{e,a}^{\text{eff}}) \\ &= S_v J_{0,a} (\rho_{i,a}^{\text{eff}} + \rho_{e,a}^{\text{eff}}) \left\{ \frac{y_{H_2}}{y_{H_2}'} \exp\left(\frac{\beta z F \eta_a}{RT}\right) - \frac{1 - y_{H_2}}{1 - y_{H_2}'} \exp\left(-\frac{(1 - \beta) z F \eta_a}{RT}\right) \right\} \end{aligned} \quad (8)$$

**2.1.2 Overpotential Due to Mass Transport.** Diffusion processes within a porous electrode structure can be distinguished as two types. First, there is normal diffusion in which one gas diffuses through another, with negligible influence of the pore walls on the rate of diffusion. This applies when the mean free path of the molecules is much less than the pore diameter. **Second, when the mean free path of the molecules is greater than the pore diameter, this is referred to as Knudsen diffusion. For most of SOFCs, the Knudsen effects cannot be neglected [14].** Therefore, for a binary gas system going through the pore structure, the overall effective diffusion coefficient  $D_i^{\text{eff}}$  can be written by combining effective normal binary diffusion coefficient  $D_{ij}^{\text{eff}}$  and the effective Knudsen diffusion coefficient  $D_{i,K}^{\text{eff}}$  [15] as in

$$\frac{1}{D_i^{\text{eff}}} = \frac{1}{D_{ij}^{\text{eff}}} + \frac{1}{D_{i,K}^{\text{eff}}} \quad (9)$$

The effective diffusion coefficient depends on the microstructure of the porous anode, quantified through the porosity and tortuosity

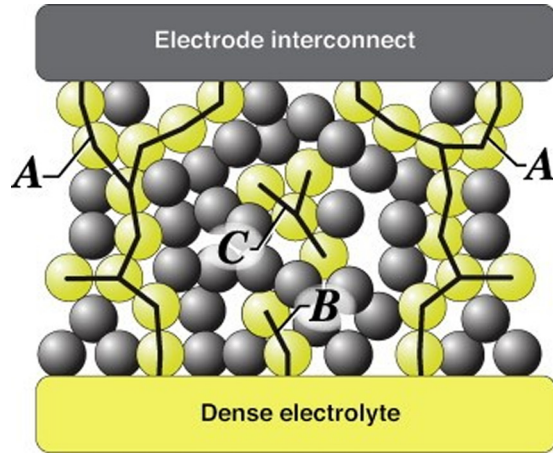


Fig. 1 Percolation threshold in the electrode

values. Thus, the effective binary diffusion coefficient can be written as

$$D_{i,j}^{\text{eff}} = \frac{\varepsilon}{\tau} D_{i,j} \quad (10)$$

For Knudsen diffusion, the coefficient can be described as in [1]

$$D_{i,K} = \frac{2}{3} d_0 \sqrt{\frac{8RT}{\pi M_i}} \quad (11)$$

where  $d_0$  is the pore diameter (m) and is assumed to be approximately proportionate to the hydraulic diameter [16]

$$d_0 \approx d_h \frac{4}{A_0} \frac{\varepsilon}{1 - \varepsilon} \quad (12)$$

$A_0$  is the specific surface area based on the solid volume. For randomly packed binary spheres,  $A_0$  is expressed as

$$A_0 = \frac{6}{d_e} \frac{n_e + (1 - n_e)\alpha^{-2}}{n_e + (1 - n_e)\alpha^{-3}} \quad (13)$$

where  $d_e$  is the diameter (m) of electrically conducting particles,  $\alpha$  is the particle size ratio of ionic to electronic conducting particles.

Similarly as the effective binary diffusion coefficient, the effective Knudsen diffusion coefficient can be expressed as

$$D_{i,K}^{\text{eff}} = \frac{\varepsilon}{\tau} D_{i,K} \quad (14)$$

The general form of the Fick's law takes into account both diffusion and convection mass transfer and can be expressed as [17]

$$N_{H_2} = -D_{H_2}^{\text{eff}} \frac{dc_{H_2}}{dx} + c_{H_2} v \quad (15)$$

$$N_{H_2O} = -D_{H_2O}^{\text{eff}} \frac{dc_{H_2O}}{dx} + c_{H_2O} v \quad (16)$$

where  $N_i$  is molar flux (mol/m<sup>2</sup> s) of species  $i$ ,  $D_i^{\text{eff}}$  is the effective diffusion coefficient (m<sup>2</sup>/s) of species  $i$  (from Eq. (9)),  $c_i$  is the concentration (mol/m<sup>3</sup>) of specie  $i$ , and  $v$  is the convection velocity (m/s).

Under constant operating temperatures, the ideal gas law can be written as

$$\frac{dp}{dx} = -\frac{dc}{dx} RT \quad (17)$$

If pressure is uniform throughout the electrode, then  $dp/dx$  is constant. According to Eq. (17),  $dc/dx$  will also be constant. Then we will have

$$\frac{dc_{H_2}}{dx} = -\frac{dc_{H_2O}}{dx} \quad (18)$$

For equimolar counter-current mass transfer, we have  $N_{H_2} = -N_{H_2O}$ . Combine this condition with Eqs. (15) and (16). The  $H_2$  flux can be expressed as

$$N_{H_2} = -\left(y_{H_2O} D_{H_2}^{\text{eff}} + y_{H_2} D_{H_2O}^{\text{eff}}\right) \frac{dc_{H_2}}{dx} \quad (19)$$

Based on flux-current relations as well as ideal gas law, we have

$$N_{H_2} = \frac{J_{e,a}}{2F} \quad (20a)$$

$$\frac{dc_{H_2}}{dx} = \frac{dy_{H_2}}{dx} \frac{P}{RT} \quad (20b)$$

Then Eqs. (20) turn into

$$\frac{dy_{H_2}}{dx} = -\frac{1}{(1 - y_{H_2})D_{H_2}^{\text{eff}} + y_{H_2}D_{H_2O}^{\text{eff}}} \frac{RT J_{e,a}}{P} \quad (21)$$

**2.1.3 Anode Governing Equations and Boundary Conditions.** Combining the equations and solving for the molar fraction of fuel, electronic current density, and overall overpotential, we get a total of three governing equations for the anode given by

$$\begin{aligned} \frac{d^2 \eta_a}{dx^2} = & S_v J_{0,a} \left( \rho_{i,a}^{\text{eff}} + \rho_{e,a}^{\text{eff}} \right) \left\{ \frac{y_{H_2}}{y_{H_2}'} \exp\left(\frac{\beta z F \eta_a}{RT}\right) \right. \\ & \left. - \frac{1 - y_{H_2}}{1 - y_{H_2}'} \exp\left(-\frac{(1 - \beta) z F \eta_a}{RT}\right) \right\} \end{aligned}$$

$$\frac{dJ_{e,a}}{dx} = -S_v J_{0,a} \left\{ \frac{y_{H_2}}{y_{H_2}'} \exp\left(\frac{\beta z F \eta_a}{RT}\right) - \frac{1 - y_{H_2}}{1 - y_{H_2}'} \exp\left(-\frac{(1 - \beta) z F \eta_a}{RT}\right) \right\}$$

$$\frac{dy_{H_2}}{dx} = -\frac{1}{(1 - y_{H_2})D_{H_2}^{\text{eff}} + y_{H_2}D_{H_2O}^{\text{eff}}} \frac{RT J_{e,a}}{P}$$

The computational domain is shown in Fig. 2. The boundary conditions for the governing equations can be derived as follows: at the fuel gas inlet, which is also the location of the current collector, the hydrogen molar fraction is equal to the bulk flow value. The total current density only comes from the transport of electrons. As a result, the boundary conditions can be expressed as

$$y_{H_2}|_{\text{inlet}} = y_{H_2}(\text{bulk})$$

$$J_{i,a}|_{\text{inlet}} = 0$$

$$J_{e,a}|_{\text{inlet}} = J_{\text{total}}$$

$$\frac{d\eta_a}{dx}|_{\text{inlet}} = \rho_{i,a}^{\text{eff}} J_{i,a} - \rho_{e,a}^{\text{eff}} J_{e,a} = -\rho_{e,a}^{\text{eff}} J_{\text{total}}$$

At the electrode–electrolyte (EE) interface, the transport of ions is the only factor that contributes to the overall current density.

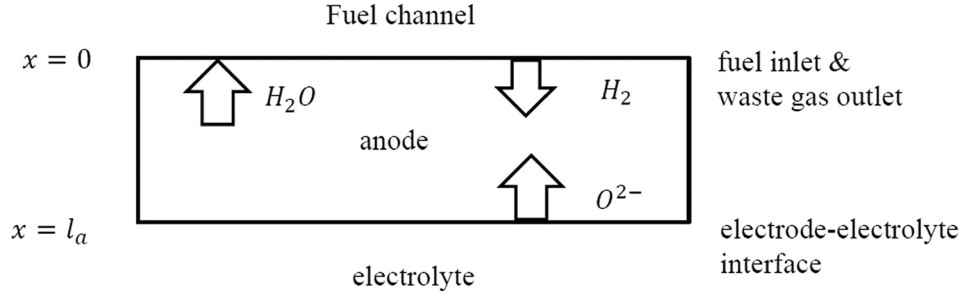


Fig. 2 Anode computational domain

Therefore, ion current density equals to the overall current density. This defines the boundary condition of the overpotential at the EE interface

$$J_{i,a}|_{EE} = J_{\text{total}}$$

$$\frac{d\eta_a}{dx}|_{EE} = \rho_{i,a}^{\text{eff}} J_{i,a} - \rho_{e,a}^{\text{eff}} J_{e,a} = \rho_{i,a}^{\text{eff}} J_{\text{total}}$$

After solving the three coupled governing equations,  $\eta_a$ ,  $J_{e,a}$ , and  $y_{H_2}$  distributions can be obtained. Now the overall overpotential of the anode can be written as follows:

$$\eta_a|_{\text{overall}} = (V_e^{\text{eq}} - V_i^{\text{eq}}) - (V_e|_{\text{inlet}} - V_i|_{EE}) = \eta_a|_{\text{inlet}} + \eta_a|_{EE} \quad (22)$$

## 2.2 Cathode

**2.2.1 Overpotential Due to Electrochemical Reactions and Ohmic Resistance.** The electrochemical reaction equations in the cathode are similar to the ones in the anode and can be derived in a similar fashion, to produce the following:

$$\frac{d^2\eta_c}{dx^2} = S_v J_{0,c} (\rho_{i,c}^{\text{eff}} + \rho_{e,c}^{\text{eff}}) \times \left\{ \frac{y_{O_2}}{y'_{O_2}} \exp\left(\frac{\beta z F \eta_c}{RT}\right) - \exp\left(-\frac{(1-\beta) z F \eta_c}{RT}\right) \right\} \quad (23)$$

$$\frac{dJ_{e,c}}{dx} = -S_v J_{0,c} \left\{ \frac{y_{O_2}}{y'_{O_2}} \exp\left(\frac{\beta z F \eta_c}{RT}\right) - \exp\left(-\frac{(1-\beta) z F \eta_c}{RT}\right) \right\} \quad (24)$$

where  $\eta_c$  is the cathode overpotential,  $J_{0,c}$  is the cathode exchange current density,  $\rho_{e,c}^{\text{eff}}$  is the effective resistivity of cathode electrically conducting particles, and  $J_{e,c}$  is the electronic current density.

**2.2.2 Overpotential Due to Mass Transport.** Following the derivation in Ref. [17], an effective Knudsen diffusion coefficient of  $O_2$  can be defined as

$$N_{O_2} = -D_{O_2,K}^{\text{eff}} \left( \frac{dc_{O_2}}{dx} \right)_{\text{Knudsen}} \quad (25)$$

The effective normal diffusion of oxygen taking both conduction and convection transport can be defined by

$$N_{O_2} = -D_{O_2,N_2}^{\text{eff}} \left( \frac{dc_{O_2}}{dx} \right)_{\text{normal}} + c_{O_2} v$$

$$= -D_{O_2,N_2}^{\text{eff}} \left( \frac{dc_{O_2}}{dx} \right)_{\text{normal}} + c_{O_2} \frac{N_{\text{total}}}{c_{\text{total}}} \quad (26)$$

Total concentration of  $O_2$  is equal to the summation of Knudsen concentration and normal concentration

$$\frac{dc_{O_2}}{dx} = \left( \frac{dc_{O_2}}{dx} \right)_{\text{Knudsen}} + \left( \frac{dc_{O_2}}{dx} \right)_{\text{normal}}$$

$$= - \left( \frac{1}{D_{O_2,K}^{\text{eff}}} + \frac{1}{D_{O_2,N_2}^{\text{eff}}} \right) N_{O_2} + \frac{c_{O_2}}{c_{\text{total}}} \frac{1}{D_{O_2,N_2}^{\text{eff}}} N_{\text{total}} \quad (27)$$

On the cathode side, nitrogen does not involve any electrochemical reaction, so flux of nitrogen at steady state is zero leading to  $N_{\text{total}} = N_{O_2}$ . The  $O_2$  flux turns into

$$N_{O_2} = - \left( \frac{1}{D_{O_2,K}^{\text{eff}}} + \frac{1-y_{O_2}}{D_{O_2,N_2}^{\text{eff}}} \right)^{-1} \frac{dc_{O_2}}{dx} \quad (28)$$

By combining flux-current relations and the ideal gas law, Eq. (28) becomes

$$\frac{dy_{O_2}}{dx} = - \frac{RT}{P} \left( \frac{1}{D_{O_2,K}^{\text{eff}}} + \frac{1-y_{O_2}}{D_{O_2,N_2}^{\text{eff}}} \right) \frac{J_{e,c}}{4F} \quad (29)$$

**2.2.3 Cathode Governing Equations and Boundary Conditions.** Similar to the anode, three coupled governing equations for the cathode can be defined:

$$\frac{d^2\eta_c}{dx^2} = S_v J_{0,c} (\rho_{i,c}^{\text{eff}} + \rho_{e,c}^{\text{eff}}) \times \left\{ \frac{y_{O_2}}{y'_{O_2}} \exp\left(\frac{\beta z F \eta_c}{RT}\right) - \exp\left(-\frac{(1-\beta) z F \eta_c}{RT}\right) \right\}$$

$$\frac{dJ_{e,c}}{dx} = -S_v J_{0,c} \left\{ \frac{y_{O_2}}{y'_{O_2}} \exp\left(\frac{\beta z F \eta_c}{RT}\right) - \exp\left(-\frac{(1-\beta) z F \eta_c}{RT}\right) \right\}$$

$$\frac{dy_{O_2}}{dx} = - \frac{RT}{P} \frac{1-y_{O_2}}{D_{O_2}^{\text{eff}}} \frac{J_{e,c}}{4F}$$

The boundary conditions in the cathode can also be obtained using the same approach used with the anode

$$y_{O_2}|_{\text{inlet}} = y_{O_2}(\text{bulk})$$

$$J_{i,c}|_{\text{inlet}} = 0$$

$$J_{e,c}|_{\text{inlet}} = J_{\text{total}}$$

$$\frac{d\eta_c}{dx}|_{\text{inlet}} = \rho_{i,c}^{\text{eff}} J_{i,c} - \rho_{e,c}^{\text{eff}} J_{e,c} = -\rho_{e,c}^{\text{eff}} J_{\text{total}}$$

$$J_{i,c}|_{EE} = J_{\text{total}}$$

$$\frac{d\eta_c}{dx}|_{EE} = \rho_{i,c}^{\text{eff}} J_{i,c} - \rho_{e,c}^{\text{eff}} J_{e,c} = \rho_{i,c}^{\text{eff}} J_{\text{total}}$$



After solving the governing equations, the cathode overall overpotential can be calculated as

$$\eta_c|_{\text{overall}} = (V_e^{\text{eq}} - V_i^{\text{eq}}) - (V_e|_{\text{inlet}} - V_i|_{\text{EE}}) = \eta_c|_{\text{inlet}} + \eta_c|_{\text{EE}} \quad (30)$$

### 3 Analysis of Microstructure Parameters Correlations and Percolation Threshold

**3.1 Relationship Between Porosity and Tortuosity.** Figure 3 plots the data from the experiments of Currie [9] for mixtures of spherical particles. The tortuosity ( $\tau$ ) is assumed to be inversely proportional to porosity ( $\varepsilon$ ). By applying Eq. (31) as the relationship, it can be observed from Fig. 3 that most of the data fall in the region where the  $n$ -value is between 0.4 and 0.5.

$$\tau = \frac{1}{\varepsilon^n} \quad (31)$$

In order to further investigate the adjustable parameter  $n$ , Dias et al. [10] performed an experimental study of binary mixtures of spherical particles, as shown in Fig. 4. In this figure,  $\phi_L$  represents volume fraction of large particles. It can be observed that for particle size ratios that are less or equal to 3.33, the value of  $n$  is approximately 0.5 regardless of the volume fraction. For most SOFCs, the sizes of ionic and electronic conductors are comparable, so it is reasonable to choose a value of  $n$  to be equal to 0.5 in the numerical model. However, if we happen to encounter a large particle size ratio, the plot in Fig. 4 will be used for selecting the appropriate  $n$  value. It should be noted that tortuosity is essentially a function of both porosity and particle size ratio.

**3.2 Relationship Between Porosity and Particle Size.** For common SOFCs, the particle sizes of electronic and ionic conductors will be close, and hence the ratio will be close to 1. Yerazunis et al. [18] performed experiments to analyze the binary spherical mixtures with comparable particle sizes as shown in Fig. 5. The particles were densely packed to ensure good connection of particles, as in most electrode configurations of SOFCs. Based on the experimental data, porosity can be expressed as a function of particle size ratio and volume fraction as shown in the following equation:

$$1 - \varepsilon = \frac{0.64}{1 - \left(0.362 - 0.315 \left(\frac{D_s}{D_L}\right)^{0.7}\right) \phi_L + 0.955 \left(\frac{D_s}{D_L}\right)^4 \left(\frac{\phi_L^2}{1 - \phi_L}\right)} \quad (32)$$

where  $\phi$  is volume fraction, and the subscript  $L$  and  $S$  indicates the larger particle size and smaller particle size, respectively. It

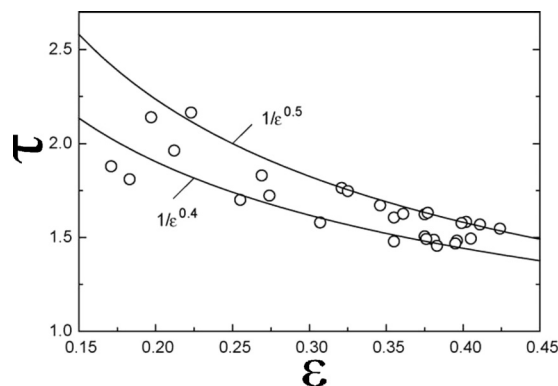


Fig. 3 Dependence of tortuosity on the packing porosity [9]

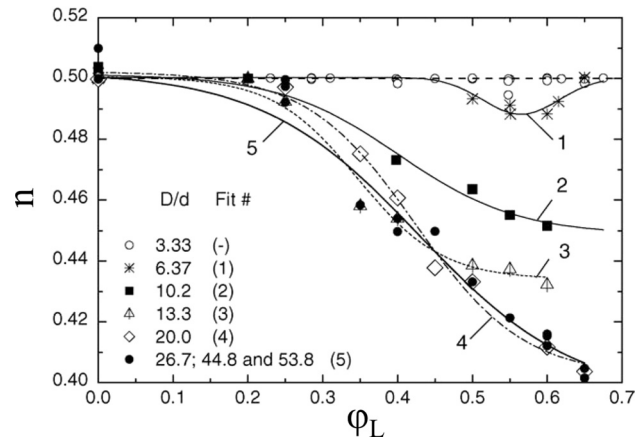


Fig. 4 Dependence of  $n$  on  $\phi_L$  for different particle size ratios [10]

can be deduced from the experimental data that the porosity value approaches 0.36 as the particle size ratio approaches 1. Therefore, we assume that when ionic particle size is equal to electronic particle size, the porosity is set to be 0.36. It is noted that in this particular circumstance bimodal mixtures can be expressed as monomodal.

**3.3 Percolation Threshold.** Binary packing model is developed based on taking consideration of both coordination number theory and percolation threshold. Since in reality it is extremely hard to quantitatively measure the overall cell structure, coordination number theory can be applied to quantify the packing of electronic and ionic particles. After the packing type of the conductors throughout the electrodes is known, the next step is to use percolation threshold to determine if the packing type can result in a good conductivity to transfer the ion and electrons. In this work,

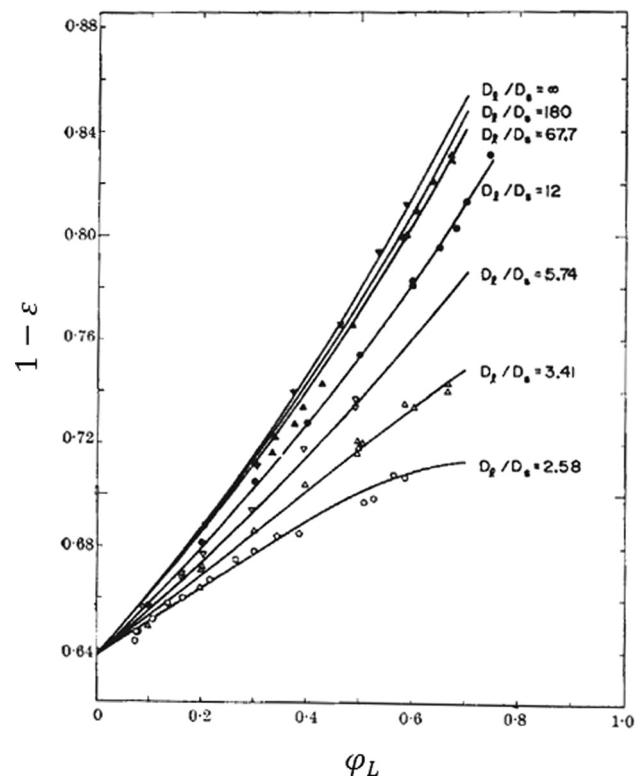


Fig. 5 Packing density versus composition for different particle size ratios [18]

percolation threshold is quantified by using the probability parameter from Eq. (34), and essentially it is a function of volume fraction (or number fraction) and particle size ratio. The value of probability needs to be greater than 0 (will also be less than 1 if greater than 0 is satisfied [7]) in order to let same type of particles form a bridge throughout the electrode to ensure good conductivity. Therefore, the model assumption will be valid only if the probability is in between 0 and 1. Otherwise, the conductivity of the cell will be extremely poor and hence results in a bad cell performance. We will not discuss those occasions since it does not have much practical significances. By knowing this information, we can use Eq. (34) to quantify percolation threshold by calculating the upper and lower boundary of particle size ratio and number fraction if volume composition of two types of conductors is given. In this model, the cell (when we talk about fuel cell in this work, we only refer to the real testing cells) was assumed to be represented as a collection of randomly packed spherical particles made up of either electronically conductive or ionically conductive materials. By applying a coordination number model [6,7] together with percolation theory, this model guarantees that the same type of particles (ionic or electronic conductors) contacts each other and forms a network or particle chain throughout the electrode to ensure good conductivity. That is to say, for any given combination of compositions and particle size ratios of electronic and ionic conductors, the coordination model can be used to differentiate if it is above or below the percolation threshold. If above the percolation threshold, pathways are guaranteed to be formed through the electrode for the conduction of ions and electrons. If below the percolation threshold, these pathways are not guaranteed to span the entire electrode and may not provide continuous pathways for conduction. In these cases, the model assumptions are not valid.

#### 4 Model Validation

In order to determine if the correlations of microstructure parameters have the potential to accurately predict cell performance, model validation was carried out. Three experimental investigations from literature [19–21] focusing on different perspectives of SOFC performance were selected to facilitate the comparison between predicted results and experimental data.

There are two types of inputs to the model: operational inputs and physical inputs. The operational inputs of the model include: operating temperature and pressure, fuel gas composition, and current density. The physical inputs include: exchange current density, thicknesses of the anode, cathode and electrolyte, volume fraction (or mass fraction) of electronic and ionic conductors, particle size of electronic (or ionic) conductors, particle size ratio of ionic to electronic conductors, porosity, and tortuosity.

The first experimental data selected are from Ref. [19]. The objective of the experiment was to investigate the effect of impregnation of different volume fractions of nanosized yttria-stabilized zirconia (YSZ) particles into nickel anodes on the electrode behavior. The anodes were sintered at 1400 °C for 2 hrs, the impregnated sample was heat treated at 850 °C for 1 hr, and data were collected under stable condition at the operating temperature. Table 1 lists the parameters provided by the experimental study. In order to solve this problem using the developed numerical model, Ni particle size, tortuosity, and anode exchange current density needed to be determined.

Let us take the Ni + 4.0 mg/cm<sup>2</sup> YSZ case, for example. The volume fraction of Ni/YSZ for Ni + 4.0 mg/cm<sup>2</sup> YSZ is given as 79% Ni/21% YSZ. The number fraction of the electronic conductor can be expressed as a function of particle size ratio from Eq. (33). The probability that one cluster that belongs to a percolation cluster can be obtained from Eq. (34). Then the upper and lower bounds of particle size ratio and electronic number fraction are calculated to make probability parameter fall in between 0 and 1. And the results are listed in Table 2. The values within the two

bounds will maintain percolation and hence ensure good conductivity

$$\varphi_e = \frac{n_e}{(1 - n_e)\alpha^3 + n_e} \quad (33)$$

$$P_e = \left[ 1 - \left( \frac{4 - Z_{e-e}}{2} \right)^{2.5} \right]^{0.4} \quad (34a)$$

$$P_i = \left[ 1 - \left( \frac{4 - Z_{i-i}}{2} \right)^{2.5} \right]^{0.4} \quad (34b)$$

where

$$Z_{e-e} = \frac{6n_e}{[n_e + (1 - n_e)\alpha^2]}$$

$$Z_{i-i} = \frac{6n_i}{[n_i + (1 - n_i)\alpha^{-2}]}$$

Substituting the porosity value and the volume fraction of the electronic conductor into the porosity–particle size ratio correlation gives us a particle size ratio of  $\alpha = 0.4$ , which means percolation threshold clusters exist for both electronic and ionic particles. Since the scanning electron microscopy (SEM) picture is extremely vague and makes it impossible to differentiate ionic particles from electronic particles, it is reasonable to select an averaged YSZ particle size, which is 0.2  $\mu\text{m}$ , from statistical point of view. Ni particle size can be derived as 0.5  $\mu\text{m}$ . Detailed sensitivity study of particle size is performed in Sec. 5.

Tortuosity can be obtained from the porosity–tortuosity correlation. Since the particle ratio in this case is less than 3.33, it is reasonable to set  $n$  equals to 0.5.

$$\tau = \frac{1}{\varepsilon^n} = \frac{1}{0.3^{0.5}} = 1.826$$

Exchange current density was calculated from the provided electrochemical impedance spectroscopy (EIS) data, and charge transfer resistance is determined by applying the simplified B–V equation. After all the parameters applied in the model are calculated, the mathematical simulation is performed. From Fig. 6, it can be seen that the numerical results and experimental data agree reasonably well with each other.

The second experiment comes from Ref. [20]. The objective of this experiment was to investigate the performance and durability of Ni-coated YSZ anodes for intermediate temperature SOFCs. The input parameters are shown in Table 3. Please note that the testing cell is exposed at the operating temperature for 3 hrs before the experimental data were collected. Therefore, the temperature of the anode is uniform and equal to the operating temperature. From the given data, the particle size ratio can be computed using the porosity and volume fraction measured in the experiment by Eq. (32). This produces  $\alpha_a = 1.56$  and  $\alpha_c = 1.41$  for the anode and cathode particle size ratio, respectively. Applying these values to Eq. (34) shows that particle size satisfies percolation threshold for both electrodes providing good connections of the same type of particles. Since the average Ni particle size is given as 25 nm, the YSZ and lanthanum strontium manganite (LSM) particle size can be calculated as 39.0 nm and 27.6 nm using the previous calculated particle size ratio.

The anode and cathode exchange current densities are calculated by the provided EIS plot from experimental measurement. Tortuosity is calculated by using the adopted submodel correlations. After that, the current–voltage (I–V) curve is calculated by applying the mathematical model. Again, a good consistency between numerical results and experimental data for both of the operating temperatures can be seen from Fig. 7.

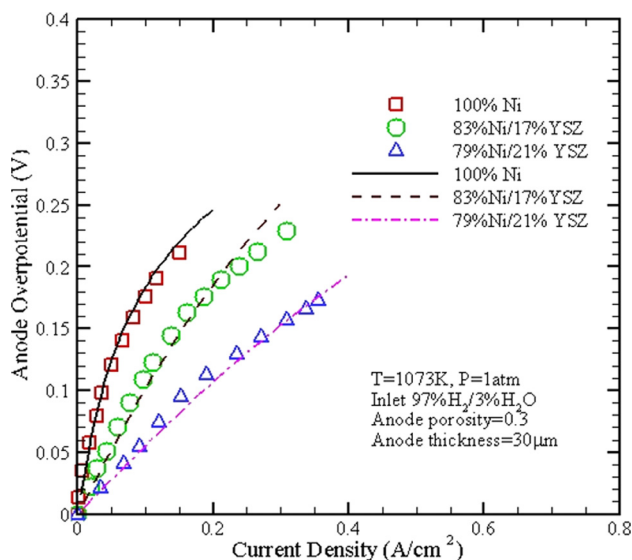
**Table 1 Value of input parameters for model validation case no. 1 [19]**

| Parameter (provided by paper) | Value  |
|-------------------------------|--|
| Operating temperature         | 1073 K   |
| Pressure                      | 1.0 atm  |
| Anode thickness               | 30 $\mu\text{m}$   |
| Electrolyte thickness         | 1 mm   |
| Anode gas composition         | 97% $\text{H}_2$ (3% $\text{H}_2\text{O}$ )  |
| Volume fraction of NiO/YSZ    | Ni: 100%/0%Ni + 2.7 mg/cm <sup>2</sup> YSZ:<br>83%/17%Ni + 4.0 mg/cm <sup>2</sup> YSZ: 79%/21% |
| Porosity                      | 30%  |
| YSZ particle size             | 0.1–0.3 $\mu\text{m}$  |

**Table 2 Upper and lower bounds for particle size ratio and electronic volume fraction for 79% Ni/21% YSZ [19]**

| $\phi_e = 0.79$ | Lower bound | Upper bound |
|-----------------|-------------|-------------|
| $\alpha$        | 0.13        | 0.53        |
| $n_e$           | 0.09        | 0.36        |

The last experimental data are from Ref. [21]. The objectives of his experiments were to examine the influence of sintering temperature on cell performance by using an anode half-cell. Pt paste was applied to the opposite side of the electrode as counter and reference electrodes. The paper provided SEM pictures of the anode microstructure at four different sintering temperatures. The input parameters are shown in Table 4. In Fig. 8, the electronic and ionic particle sizes are approximated from the SEM pictures. The dashed and solid circles are used to denote Ni and 8 mol. %  $\text{Y}_2\text{O}_3\text{-ZrO}_2$  (TZ8Y) particles, respectively. Please note that Fig. 8 is originally published in journal of ECS (Electrochemical Society) by Jiang [21]. ECS journal has granted the permission of using this figure in our work. Furthermore, TZ8Y and YSZ in this work are identical. TZ8Y will only be used in this model validation case in order to comply with the permission rules from ECS journal. Image analysis has been applied in order to estimate the electronic and ionic particle sizes by collecting and measuring the number of pixels from the SEM images provided in the experimental study. This process requires two steps. First, the electronic and ionic particles must be differentiated. Because these particles are only annotated in a few of the images, the process is

**Fig. 6 Comparison between numerical results and experimental data for case no. 1 [19]**

complicated. However, it is clear in the images that rising sintering temperature tends to increase ionic (YSZ) conductor particle size, while the electronic (nickel) conductor is minimally influenced. This distinct trend allows for consistent differentiation of electronic and ionic particles among all SEM images. Second, the pixels in the clearly identified particles are counted using a MATLAB script, and the area is measured by the given scale from the SEM images.

The range of particle size ratio that can maintain the percolation threshold is calculated to be between 0.5 and 2 for this volume fraction composition. At 1300 °C, YSZ particle size is approximately 0.5  $\mu\text{m}$ , while the Ni particle size is about 2  $\mu\text{m}$  resulting in a particle size ratio of  $\alpha = 0.25$ . Under these conditions, the assumptions of the current model break down because the percolation threshold is not satisfied. Therefore, the predicted results would not be valid. However, we can still use the closest limiting particle size ratio (i.e.,  $\alpha = 0.5$ ) to calculate an I–V curve to compare with the experimental data. For this case, the mathematical predictions should have better performance than experimental data because percolation threshold is assumed to be satisfied. This same approach is used for the 1350 °C sintering temperature case, as well, because of the extreme particle size difference of two types of conductors (0.6  $\mu\text{m}$  for Ni and 2  $\mu\text{m}$  for YSZ resulting in  $\alpha = 0.3$ ). For 1400 °C, the Ni and YSZ particle sizes are estimated as 1.25  $\mu\text{m}$  and 1.5  $\mu\text{m}$ , respectively, resulting in  $\alpha = 0.83$ . For 1500 °C, both Ni and YSZ particle sizes are estimated as 2  $\mu\text{m}$ , resulting in  $\alpha = 1$ . The particle size ratios are within the percolation threshold for the 1400 and 1500 °C sintering temperature cases and the numerical simulation can be applied. Once the particle sizes of electronic and ionic conductors are determined, the porosity is obtained by using the porosity–particle size ratio correlation. The calculated porosity is 0.4 for 1400 °C, and 0.36 for 1500 °C. Next, the discrepancy between the measured porosity and the calculated one will be compared. After performing the similar image analysis as illustrated before, the porosity can be approximated as 0.38 for 1400 °C and 0.37 for 1500 °C. The maximum discrepancy between the measured and calculated porosity value is only 5%. This also demonstrates the accuracy of the adopted submodel correlation.

Figure 9 shows the comparison of model predictions versus experimental data. It can be seen that for 1400 and 1500 °C sintering temperatures, the numerical results matched reasonably well with the experimental data. However, for the remaining two sintering temperatures, there is a noticeable difference between model results and experimental data, as expected. For these cases, the numerical model calculated a scenario where particle size ratio was artificially selected to satisfy the percolation threshold. However, in reality the particle size ratio falls outside the percolation threshold range indicating poor connectivity between the particles of the ionic and electronic conductors. Therefore, observed experimental data, where the terminal voltage drops rapidly and reaches

**Table 3 Value of input parameters for model validation case no. 2 [20]**

| Parameter (provided by paper) | Value                                       |
|-------------------------------|---|
| Operating temperature         | 700 °C/800 °C                               |
| Pressure                      | 1.0 atm                                     |
| Anode thickness               | 1200 $\mu\text{m}$                          |
| Electrolyte thickness         | 7 $\mu\text{m}$                             |
| Cathode thickness             | 30 $\mu\text{m}$                            |
| Anode gas composition         | 97% $\text{H}_2$ (3% $\text{H}_2\text{O}$ ) |
| Cathode gas composition       | Air   |
| Volume fraction of NiO/YSZ    | 40%/60%                                     |
| Mass fraction of LSM/YSZ      | 50%/50%                                     |
| Porosity                      | 40%   |
| NiO particle size (anode)     | 20–30 nm                                    |
| YSZ particle size (anode)     | < 300 nm                                    |

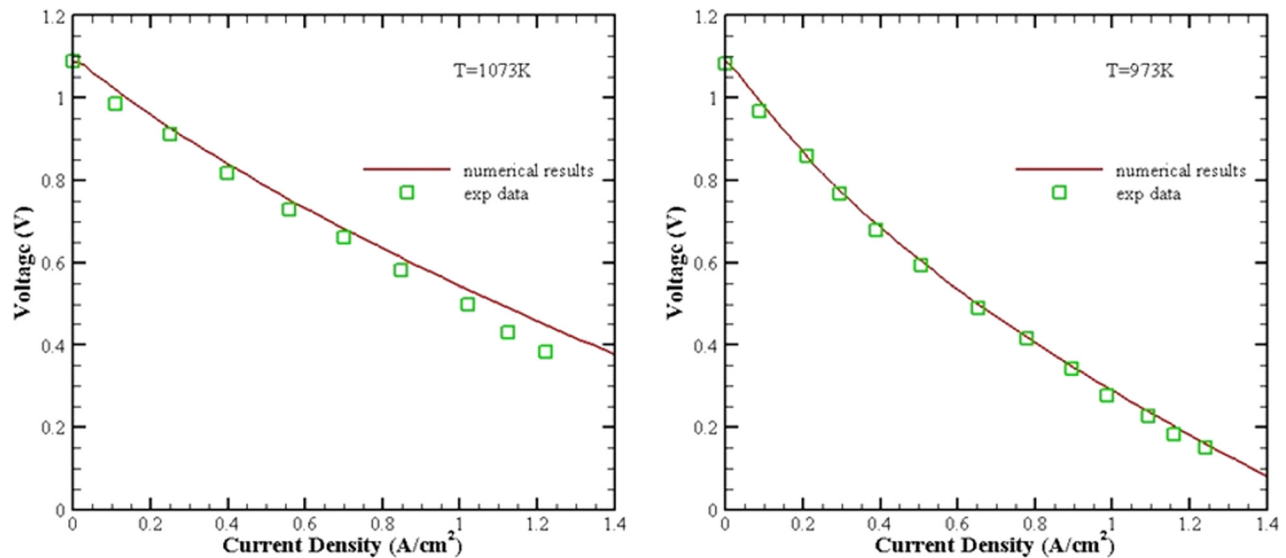


Fig. 7 Comparison between numerical results and experimental data for case no. 2 [20]

zero at a very small current density value, follow with expected behavior based on our model assumptions.

The method of calculating tortuosity in this case is a little different from the previous applications in order to better match the provided experimental results. Normally, the ohmic overpotential is smaller compared with concentration and activation overpotential in the electrodes. However, for this particular case, the ohmic overpotential is abnormally high ( $1.03 \Omega \text{ cm}^2$  for  $1400^\circ\text{C}$  and  $1.1 \Omega \text{ cm}^2$  for  $1500^\circ\text{C}$ ). Fine Pt mesh was used as the current collector for both the cermet electrode and counter electrode. The ohmic resistance coming from the current collector can be neglected because it is several order of magnitude less than the overall ohmic resistance. Since the experimental data are given for ohmic resistance, we can apply these data to calculate the tortuosity using Eq. (5). However, if the porosity–tortuosity correlation is still applied, the estimated tortuosity would be an order of magnitude below the values which correspond to the resistance measurements. By using the tortuosity calculated by Eq. (5) to approximate the concentration and activation overpotential, together with the measured ohmic resistance, it can be seen that the numerical results match the experimental data very well. Therefore, the only valid explanation is that the bad packing of particles will cause an irregular shape of microstructure and hence results in a high tortuosity and high ohmic resistance. However, for a normally well-structured fabricated cell, the porosity–tortuosity correlation is valid for predicting the cell performance as shown by previous validation cases. But this experimental study primarily focuses on how the sintering temperature affects the cell performance and is not quite meaningful for the well-structured SOFC due to the extremely poor performance. Essentially, our model will be mainly used to predict the well-structured SOFC performance. In

this work, well-structured cell indicates microstructural parameters satisfying percolation threshold throughout the electrodes. The purpose of this validation case mainly reveals how the real structure affects the numerical modeling so that we can demonstrate the feasibility and practicability of our numerical study.

## 5 Model Sensitivity Study

The model validation showed a reasonable ability to predict experimental performance results from given cell microstructural parameters. Next, a sensitivity study is performed to investigate the effect of submodel correlations on model predictions. The first experimental case from Sec. 4 is selected as a baseline. This is because the experiment has been tested and validated indicating a good consistency with the results from the numerical model. Also, it simplifies the analysis by isolating the anode half-cell. Selected variables will be varied to test the sensitivity of model predictions to these variations, while the rest of the parameters will be obtained from the experiment validation case. In the sensitivity study, two different volume fractions are selected to perform the tests in order to expand the sample sizes.

**5.1 Tortuosity Versus Porosity.** There are two places containing the tortuosity parameter in the model. They are related to ohmic resistance in electrode and mass diffusion. First of all, since electronic conductivity is several orders of magnitude higher than the ionic conductivity, ohmic overpotential is primarily dominated by the resistance due to ionic conduction. Based on Eq. (5), it can be found that increasing tortuosity will result in an increase in effective ionic resistivity and hence worsen the performance of the SOFC. Physically, this follows from the fact that as tortuosity increases, the path length for conduction from one end of the electrode to the other end increases. Second, the parameter of tortuosity also appears in the effective diffusivity to impact the gas diffusion process. From Eq. (10), it can be seen that the increase of tortuosity will result in a decrease in the effective diffusion coefficient (or a corresponding increase in mass transfer resistance). In that case, a larger tortuosity will lead to a lower concentration of fuel at EE interface and hence increases the concentration overpotential.

For this test case, the porosity is given as 30%. The idea is to vary the unknown parameter  $n$  in the porosity–tortuosity correlation given in Eq. (31) in order to find out how tortuosity impacts the model. The  $n$ -value is chosen to vary from 0.01 to 1 for 79%/21% Ni/YSZ and from 0.01 to 1.3 for 83%/17% Ni/YSZ,

Table 4 Value of input parameters for model validation case no. 3 [21]

| Parameter (provided by paper) | Value                                       |
|-------------------------------|---|
| Operating temperature         | 1273 K                                      |
| Pressure                      | 1.0 atm                                     |
| Anode thickness               | 20–40 $\mu\text{m}$                         |
| Electrolyte thickness         | $0.9 \pm 0.03 \text{ mm}$                   |
| Anode gas composition         | 97% $\text{H}_2$ (3% $\text{H}_2\text{O}$ ) |
| Volume fraction of NiO/YSZ    | 50%/50%                                     |
| NiO particle size             | Approximate from SEM                        |
| YSZ particle size             | Approximate from SEM                        |



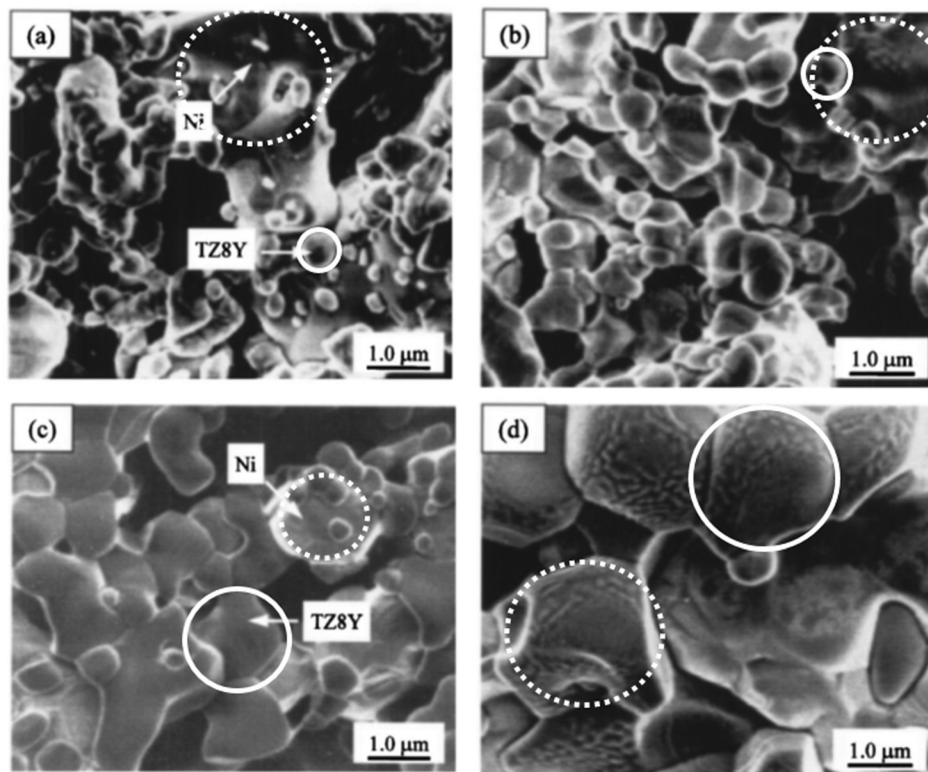


**Fig. 8** SEM picture of Ni/8 mol. %  $\text{Y}_2\text{O}_3\text{-ZrO}_2$  (Ni/TZ8Y) cermet anodes sintered at (a) 1300 °C, (b) 1350 °C, (c) 1400 °C, and (d) 1500 °C. (Reprinted with permission from Jiang [21]. Copyright 2003 by Journal of the Electrochemical Society.)

respectively. The overpotential values calculated from the corresponding varying  $n$ -values are compared with the baseline experimental data, which are represented by the model with  $n=0.5$  (which were used for the model validation case). The purpose is to explore how the  $n$ -value affects the predicted anode overpotential. Figure 10 shows a plot of tortuosity (which is a function of  $n$ ) versus the %-error difference when compared with the baseline experimental data (i.e.,  $n=0.5$ ). The dashed region indicates the

range of  $\pm 5\%$  difference between the predicted and experimental values of anode overpotential. In order to maintain the predicted overpotential between the 5% error bars, the range of the  $n$ -value is approximately from 0.275 to 0.685 for 79%/21% Ni/YSZ and from 0.08 to 0.79 for 83%/17% Ni/YSZ, respectively. Correspondingly, the tortuosity value and percentage range are about 1.4–2.25 (–23.3% to 33.7%) for 79%/21% Ni/YSZ, and 1.1–2.5 (–39.6% to 36.9%) for 83%/17% Ni/YSZ. This illustrates that a relatively large variation in the tortuosity value ( $\sim \pm 40\%$ ) results in a small impact on the predicted overpotential ( $\pm 5\%$ ).

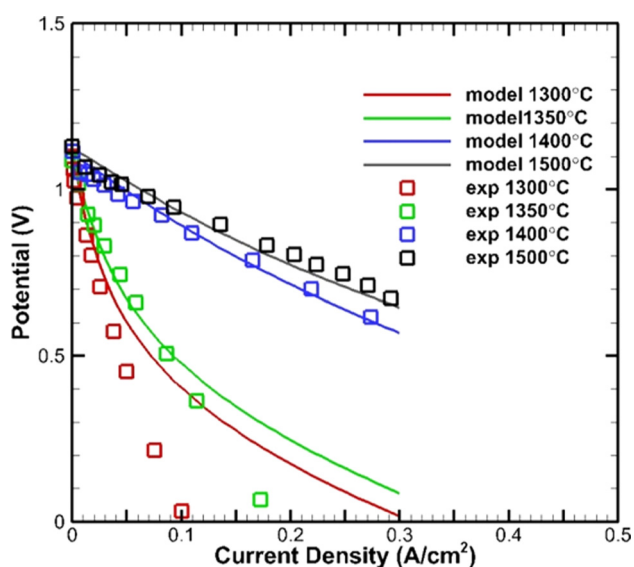


**Fig. 9** Comparison between numerical results and experimental data for case no. 3 [21]

**5.2 Particle Size Ratio Versus Porosity.** The anode governing equations indicate that both mass diffusion and electrochemical reaction rate depend on the particle size ratio. For 79%/21% volume fraction Ni/YSZ, the range of particle size ratio is calculated to be between 0.13 and 0.53 to maintain percolation threshold. For 83%/17% volume fraction Ni/YSZ, the range of particle size ratio is calculated to be between 0.1 and 0.4 to maintain percolation threshold. This means that the ionic conducting particles will always be smaller than the electronic conducting particles for this case. Based on the calculation from the numerical model, it can be found that as the particle size ratio increases (getting closer to 1), the active surface area decreases and results in an increase in cell overpotential as shown in Fig. 11. This is because as particle size ratio ( $\alpha = r_i/r_e$ ) gets smaller (ionic particles get smaller or electronic particles get larger), the size difference of two types of conductors is expected to be more significant. Therefore, electrochemical reactions rate will be boosted by increased contact area between the electronic and ionic conducting materials at the triple phase boundary region and hence improve the cell performance. For mass transfer, as particle size ratio increases (getting closer to 1), the diffusion coefficient will get smaller based on Eqs. (11)–(13), leading to an increase in the concentration overpotential. However, in this case, the particle size ratio impact for gas

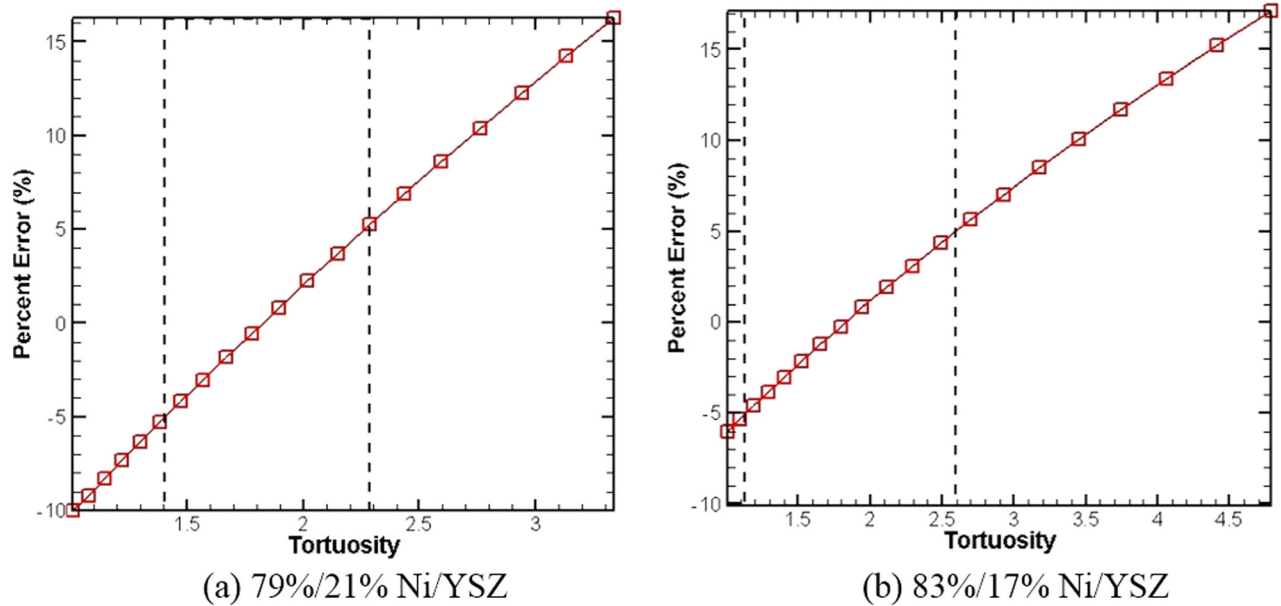


Fig. 10 Comparison of predicted anode overpotential at different  $n$ -values

diffusion is not as significant due to an extremely thin anode thickness.

For both of the test volume fractions, the varying factor will be particle size ratio only. The particle size ratio is chosen to vary from 0.35 to 0.44 for 79%/21% Ni/YSZ, and the experimental data are represented by selecting  $\alpha = 0.4$ , which were used for the model validation case. For 83%/17% Ni/YSZ, the particle size ratio is varied from 0.34 to 0.4, and the experimental data are represented again by the  $\alpha$  value used for the validation case, which were 0.382. As shown in Fig. 12, if the overpotential difference between numerical results and experimental data is expected to be within 5% error (dashed line region), the deviation of particle size ratio and its percentage needs to be 0.386–0.414 (−3.5% to 3.5%) for 79%/21% Ni/YSZ, and 0.376–0.385 (−1.3% to 1.1%) for 83%/17% Ni/YSZ, respectively. For both of the two volume fractions, the model performance predictions are strongly sensitive to the particle size ratio.

**5.3 Discussion.** To summarize, Table 5 lists the results of the sensitivity study for the submodel correlations at two different volume fractions. It can be seen that the model is extremely sensitive to the porosity–particle size ratio correlation. These parameters can only be deviated within a narrow range, which is within  $\pm 3.5\%$  in order to maintain a  $\pm 5\%$  variation in the predicted overpotential for both of the volume fraction cases. Therefore, it is critical that this value is accurately determined and represented in the model. Image analysis can be employed to measure the particle sizes if a clear and high resolution SEM image can be obtained. Some experimental approaches and equipment can also help to accurately measure and even stabilize the particle size, such as laser diffraction, 3D tomography, and focused ion beam SEM technique. However, the model does not seem to be very sensitive to the porosity–tortuosity correlation. For a small variation in the predicted overpotential ( $\pm 5\%$ ), the tortuosity can have a deviation of up to  $\pm 20\%$  to  $\pm 30\%$ . Therefore, the

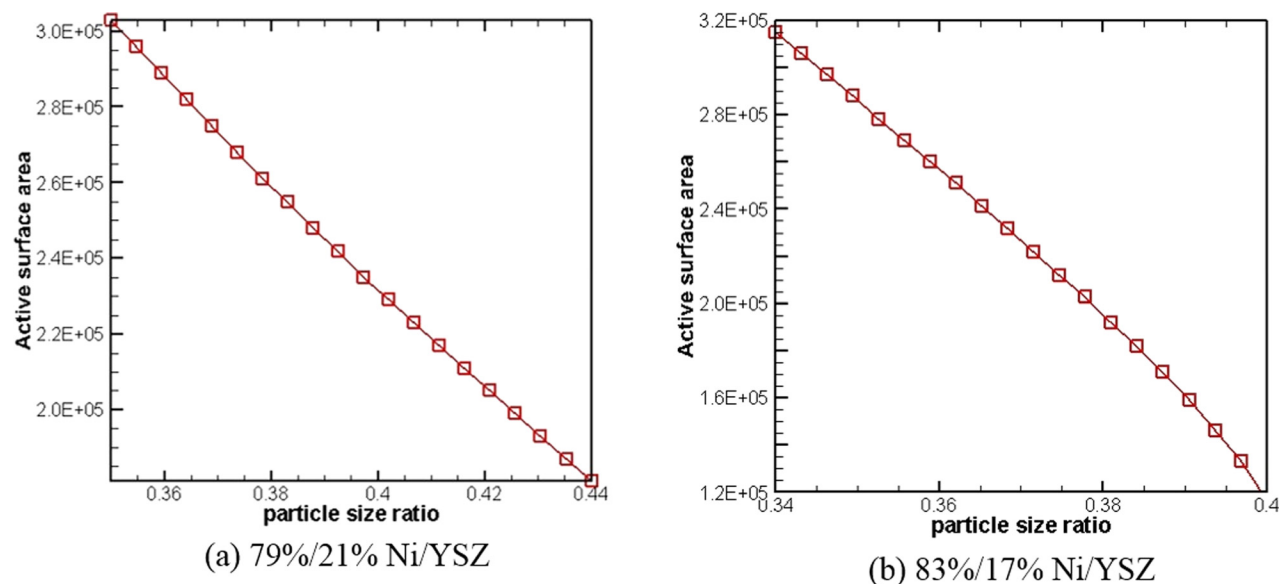


Fig. 11 Effect of particle size ratio on active surface area

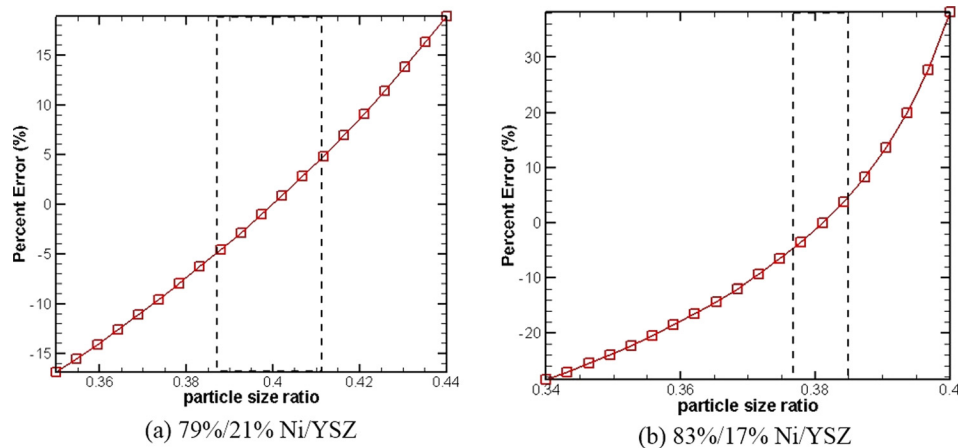


Fig. 12 Comparison of predicted anode overpotential at different particle size ratio values

Table 5 Results of sensitivity study

| Percent change corresponding to $\pm 5\%$ change in predicted overpotential compared with experimental data |                 |                 |
|---|-----------------|-----------------|
| Sample  | 79% Ni/21% YSZ  | 83% Ni/17% YSZ  |
| Tortuosity  | -23.3% to 33.7% | -39.6% to 36.9% |
| Particle size ratio   | -3.5% to 3.5%   | -1.3% to 1.1%   |

porosity–tortuosity correlation adapted here should be valid to approximate tortuosity for model predictions.

## 6 Conclusion

In this study, SOFC performance was investigated numerically by applying two submodel correlations (porosity–tortuosity and porosity–particle size ratio) aiming to tie microstructural parameters to physically measurable parameters. The model was validated against available experimental data and demonstrated the potential to predict real SOFC performance numerically rather than spending tremendous time on performing expensive experiments. The sensitivity analysis was performed on the adopted submodel correlations. It was determined that the porosity–particle size ratio correlation had a greater effect on predicted cell performance results than the porosity–tortuosity correlation. Since the model has the capability to differentiate which microstructural parameter plays a more important role in affecting the cell performance, we can take advantage of that to facilitate the experimental study of SOFC. For the parameters with noticeable sensitivity (such as particle size), they should be highlighted and noted for accurate measurement during experimental analysis. In contrast, for the parameters with trivial sensitivity (such as tortuosity), the significance may be neglected and perhaps approximate value may be used in the analysis. Furthermore, the model can also be employed to assist the design optimization study. For example, the proposed model can be used to explore FGEs in SOFC. By taking the model correlations into account, porosity grading (which can also be treated as particle size grading since these two microstructure parameters are physically connected) can be used to boost the electrochemical reactions and facilitate porous mass transfer. Using this model to study FGEs will be more reliable and accurate, since the model we adopted is more realistic and can resemble most of the real-world cell performance.

## Acknowledgment

The authors would like to acknowledge the support of the Air Force Research Laboratory (AFRL) at Wright-Patterson Air Force

Base (WPAFB) through the Wright State University Center of Advanced Power and Energy Conversion (CAPEC).

## References

- [1] Zhu, H., Kee, R. J., Janardhanan, V. M., Deutschmann, O., and Goodwin, D. G., 2005, "Modeling Elementary Heterogeneous Chemistry and Electrochemistry in Solid-Oxide Fuel Cells," *J. Electrochem. Soc.*, **152**(12), pp. A2427–A2440.
- [2] Greene, E. S., Chiu, W. K. S., and Medeiros, M. G., 2006, "Mass Transfer in Graded Microstructure Solid Oxide Fuel Cell Electrodes," *J. Power Sources*, **161**(1), pp. 225–231.
- [3] Ni, M., Leung, M. K. H., and Leung, D. Y. C., 2007, "Micro-Scale Modelling of Solid Oxide Fuel Cells With Micro-Structurally Graded Electrodes," *J. Power Sources*, **168**(2), pp. 369–378.
- [4] Chan, S. H., and Xia, Z. T., 2001, "Anode Micro Model of Solid Oxide Fuel Cell," *J. Electrochem. Soc.*, **148**(4), pp. A388–A394.
- [5] Chan, S., Khor, K., and Xia, Z., 2001, "A Complete Polarization Model of a Solid Oxide Fuel Cell and Its Sensitivity to the Change of Cell Component Thickness," *J. Power Sources*, **93**(1), pp. 130–140.
- [6] Bouvard, D., and Lange, F. F., 1991, "Relation Between Percolation and Particle Coordination in Binary Power Mixture," *Acta Metall. Mater.*, **39**(12), pp. 3083–3090.
- [7] Costamagna, P., Costa, P., and Antonucci, V., 1998, "Micro-Modeling of Solid Oxide Fuel Cell Electrodes," *Electrochim. Acta*, **43**(3–4), pp. 375–394.
- [8] Matyka, M., Khalili, A., and Koz, Z., 2008, "Tortuosity-Porosity Relation in the Porous Media Flow," *Phys. Rev. E*, **79**, p. 026306.
- [9] Currie, J. A., 1960, "Gaseous Diffusion in Porous Media. Part 2—Dry Granular Materials," *Br. J. Appl. Phys.*, **11**(8), pp. 318–324.
- [10] Dias, R., Teixeira, J., Mota, M., and Yelshin, A., 2006, "Tortuosity Variation in a Low Density Binary Particulate Bed," *Sep. Purif. Technol.*, **51**(2), pp. 180–184.
- [11] German, R. M., 1989, *Particle Packing Characteristics*, Metal Powder Industry, Princeton, NJ.
- [12] Dias, R. P., Teixeira, J. A., Mota, M. G., and Yelshin, A. I., 2004, "Particulate Binary Mixtures: Dependence of Packing Porosity on Particle Size Ratio," *Ind. Eng. Chem. Res.*, **43**(24), pp. 7912–7919.
- [13] O'Hayre, R., Cha, S.-W., Colella, W., and Prinz, F. B., 2009, *Fuel Cell Fundamentals*, 2nd ed., Wiley, Hoboken, NJ.
- [14] Lee, W. Y., Wee, D., and Ghoniem, A. F., 2009, "An Improved One-Dimensional Membrane-Electrode Assembly Model to Predict the Performance of Solid Oxide Fuel Cell Including the Limiting Current Density," *J. Power Sources*, **186**(2), pp. 417–427.
- [15] Pollard, W. G., and Present, R. D., 1948, "On Gaseous Self-Diffusion in Long Capillary Tubes," *Phys. Rev.*, **73**(7), pp. 762–774.
- [16] Nam, J. H., and Jeon, D. H., 2006, "A Comprehensive Micro-Scale Model for Transport and Reaction in Intermediate Temperature Solid Oxide Fuel Cells," *Electrochim. Acta*, **51**(17), pp. 3446–3460.
- [17] Berger, C., 1968, *Handbook of Fuel Cell Technology*, Prentice-Hall, Upper Saddle River, NJ.
- [18] Yerazunis, S., Cornell, S. W., and Wintner, B., 1965, "Dense Random Packing of Binary Mixtures of Spheres," *Nature*, **207**(4999), pp. 835–837.
- [19] Jiang, S. P., Wang, W., and Zhen, Y. D., 2005, "Performance and Electrode Behaviour of Nano-YSZ Impregnated Nickel Anodes Used in Solid Oxide Fuel Cells," *J. Power Sources*, **147**(1–2), pp. 1–7.
- [20] Kim, S., Moon, H., Hyun, S., Moon, J., Kim, J., and Lee, H., 2006, "Performance and Durability of Ni-Coated YSZ Anodes for Intermediate Temperature Solid Oxide Fuel Cells," *Solid State Ionics*, **177**(9), pp. 931–938.
- [21] Jiang, S. P., 2003, "A Comparative Study of Fabrication and Performance of Ni/3 mol. %  $Y_2O_3$   $ZrO_2$  and Ni/8 mol. %  $Y_2O_3$   $ZrO_2$  Cermet Electrodes," *J. Electrochem. Soc.*, **150**(11), pp. E548–E559.